

New spectroscopic data on even-parity autoionization states for two-color two-step photoionization of nickel atom

Jun-Yao Zhang(张钧尧), Jing-Yi Xiong(熊静逸), Hong-Ru Zhou(周鸿儒), Cai-Hua Zhu(朱才华), Huai-Miao Sun(孙槐苗), Li-De Wang(王立德), Kai-Chen Ma(马恺宸), Jun-Jie Chai(柴俊杰), and Yun-Fei Li(李云飞)
Citation: Chin. Phys. B, 2026, 35 (**1**): 013201. DOI: 10.1088/1674-1056/adf4ae
http://cpb.iphy.ac.cn; http://iopscience.iop.org/cpb

What follows is a list of articles you may be interested in

Single and double Auger decay of 4f-ionized mercury including cascade and direct processes

Yu-Long Ma(马玉龙), Fu-Yang Zhou(周福阳), Zhen-Qi Liu(刘振旗), Yi-Zhi Qu(屈一至)
Chin. Phys. B, 2018, 27 (**6**): 063201. DOI: 10.1088/1674-1056/27/6/063201

Branching ratio and angular distribution of ejected electrons from Eu $4f^7 6p_{1/2} nd$ auto-ionizing states

Xiao-Rui Wu(武晓瑞), Li Shen(沈礼), Kai Zhang(张开), Chang-Jian Dai(戴长建), Yu-Na Yang(杨玉娜)
Chin. Phys. B, 2016, 25 (**9**): 093203. DOI: 10.1088/1674-1056/25/9/093203

The VMI study on angular distribution of ejected electrons from Eu $4f^7 6p_{1/2} 6d$ autoionizing states

Zhang Kai (张开), Shen Li (沈礼), Dong Cheng (董程), Dai Chang-Jian (戴长建)
Chin. Phys. B, 2015, 24 (**10**): 103204. DOI: 10.1088/1674-1056/24/10/103204

Branching ratios of autoionization from Eu $4f^7 6p_{1/2} 6d$ [*J*] autoionizing states

Yan Jun-Gang (闫俊刚), Shen Li (沈礼), Liang Hong-Rui (梁洪瑞), Dai Chang-Jian (戴长建)
Chin. Phys. B, 2015, 24 (**8**): 083203. DOI: 10.1088/1674-1056/24/8/083203

DATA PAPER

New spectroscopic data on even-parity autoionization states for two-color two-step photoionization of nickel atom

Jun-Yao Zhang(张钧尧)[1,2,3] Jing-Yi Xiong(熊静逸)[2], Hong-Ru Zhou(周鸿儒)[2], Cai-Hua Zhu(朱才华)[2], Huai-Miao Sun(孙槐苗)[1,2], Li-De Wang(王立德)[1,2,3], Kai-Chen Ma(马恺宸)[2], Jun-Jie Chai(柴俊杰)[1,2], and Yun-Fei Li(李云飞)[1,2,†]

[1] *National Key Laboratory of Particle Transport and Separation Technology, Tianjin* 300180, *China*
[2] *Research Institute of Physical and Chemical Engineering of Nuclear Industry, Tianjin* 300180, *China*
[3] *Tianjin Key Laboratory of Stable Isotope Materials Technology, Tianjin* 300180, *China*

(Received 28 May 2025; revised manuscript received 24 July 2025; accepted manuscript online 28 July 2025)

The development of collinear resonance ionization spectroscopy for studying the nuclear structure of nickel isotopes far from the stability line relies on high-efficiency two-color two-step photoionization pathways. We systematically investigated the even-parity autoionization spectrum of atomic nickel through resonance ionization mass spectrometry (RIMS). Fifteen intense single-color photoionization lines and corresponding transitions in the 300–325 nm range were identified and excluded as potential interference peaks for subsequent two-color studies. Fifty-one even-parity autoionization states in the 64000–66800 cm^{-1} range were identified for the first time by scanning from five intermediate excited states of the $3d^8(^3F)4s4p(^3P^o)$ configuration. Forty-eight of these states were assigned unique total angular momentum quantum numbers (J) based on electric dipole transition selection rules. The autoionization state at 64437.77 cm^{-1} was identified as an optimal final state for enhancing photoionization efficiency in two-color two-step pathways. This study provides comprehensive datasets of even-parity autoionization states of nickel, supporting both the advancement of collinear resonance ionization spectroscopy for exotic nickel isotopes and theoretical modeling of autoionization states. The datasets are openly available at https://doi.org/10.57760/sciencedb.j00113.00280.

Keywords: nickel, autoionization states, even-parity, resonance ionization mass spectrometry (RIMS)

PACS: 32.80.Zb, 82.80.Ms, 42.55.Mv

DOI: 10.1088/1674-1056/adf4ae **CSTR:** 32038.14.CPB.adf4ae

1. Introduction

Nickel ($Z = 28$), characterized by its proton magic number, spans an isotopic chain covering neutron magic numbers $N = 20$, 28, and 50, encompassing both doubly magic nuclei (e.g., ^{56}Ni, ^{78}Ni) and isotopes with extreme neutron-to-proton ratios, thereby establishing nickel as a pivotal element for probing nuclear structure and shell evolution.[1–7] The neutron-rich, doubly magic nucleus ^{78}Ni serves as a stringent test case of shell closure effects, while its shape coexistence phenomenon provides critical insights into the evolution of traditional magic numbers under extreme conditions. These unique features establish ^{78}Ni as a cornerstone for validating and advancing nuclear structure theories.[8,9] In astrophysics, nickel isotopes play an essential role in stellar nucleosynthesis, where their nuclear properties are crucial for modeling heavy-element formation. ^{56}Ni is the dominant product of supernova nucleosynthesis,[10] while ^{78}Ni is a potential r-process waiting-point nucleus.[11] Studies of the nickel isotopic chain represent a key interdisciplinary frontier in nuclear structure theory and astrophysics.

Laser spectroscopy is an indispensable tool in nuclear structure research.[12–14] By measuring isotope shifts and hyperfine structures, it provides model-independent nuclear properties, including nuclear spin, electromagnetic moments, and charge radii, crucial for characterizing unstable nuclei. Two primary techniques prevail: collinear laser spectroscopy (CLS), which uses fluorescence detection of laser-excited atoms, and resonance ionization spectroscopy (RIS), which relies on detection of photoionized ions. CLS achieves sub-GHz spectral resolution by suppressing Doppler broadening, enabling ultrahigh-precision measurements of isotope shifts and hyperfine structures. In contrast, RIS offers superior sensitivity, though with moderate spectral resolution (typically several GHz). For studying unstable nuclei in the light and medium-mass regions, high spectral resolution is often required, making CLS the preferred technique. However, as research targets move further from the stability line and nuclide yields decrease, the applicability of CLS is increasingly challenged. Over the past decade, collinear resonance ionization spectroscopy (CRIS), which combines the advantages of CLS and RIS, has achieved significant progress, enabling high-resolution and high-efficiency measurements of unstable nu-

†Corresponding author. E-mail: Ipce_liyf@mails.cneic.com.cn

© 2026 Chinese Physical Society and IOP Publishing Ltd. All rights, including for text and data mining, AI training, and similar technologies, are reserved.

clei across the light, medium, and heavy mass regions.[15–25] This makes CRIS one of the most suitable methods for studying low-yield exotic nuclei such as ^{78}Ni.

CRIS detects ions generated through collinear laser resonant ionization, which requires photoionization pathways with high efficiency. A two-color two-step photoionization pathway involves initial excitation of the target element or isotope from the ground or a metastable state to an intermediate level, followed by subsequent photon absorption to exceed the ionization threshold. This approach has been widely adopted in CRIS studies as well as in isotope separation on-line (ISOL) facilities and resonance ionization mass spectrometry (RIMS) due to its advantages in minimizing laser system complexity and improving operational simplicity compared with the three-color three-step photoionization pathway.[26–31] The primary focus of designing a two-color two-step photoionization pathway lies in the identification of optimal final excitation states, as direct non-resonant ionization from the intermediate level typically yields a low cross-section. Autoionizing states or Rydberg states are typically chosen as the final states to maximize photoionization efficiency.

Compared to the odd-parity autoionization states previously studied,[32–36] the even-parity autoionization states in atomic nickel have received limited experimental attention. To the best of our knowledge, only one systematic investigation of even-parity levels has been reported, by Lievens *et al.*,[37] who explored both single-color and two-color photoionization of Ni I within the 313–335 nm range. They identified 31 even-parity autoionizing states in the 61680–62820 cm^{-1} range by scanning from three odd-parity excited states belonging to the $3d^8(^3F)4s4p(^3P^o)$ $^3G^o$ configuration, and measured cross-sections for several strong transitions. This lack of systematic studies underscores a critical knowledge gap that higher-lying even-parity autoionization regions remain largely uncharted. Obtaining new spectroscopic data on even-parity autoionization states is essential for developing efficient two-color two-step photoionization schemes and for advancing the understanding of nickel's even-parity excitation structure. In parallel, theoretical modeling of atomic autoionization states has advanced considerably, particularly for elements with relatively simple electronic configurations.[38–42] As a transition-metal element with a more intricate autoionization state structure, nickel offers valuable energy-level data that can serve as both a benchmark and validation tool for refining theoretical approaches to atomic autoionization-state calculations.

The ionization threshold of atomic nickel has been precisely determined at 61619.77 cm^{-1}.[43] Direct two-step photoionization from the ground state requires photons with wavelengths shorter than 324.5 nm, a range beyond the second harmonic limit of Ti:sapphire lasers. Dye lasers have served as a practical alternative, capable of producing laser light in the 300–325 nm range through frequency doubling, and are still widely employed in modern ISOL facilities.[44] Resonance ionization mass spectrometry (RIMS), which combines real-time ion detection with element-selective photoionization, is regarded as the standard laser-spectroscopy technique for studying autoionization states.[45–49] In this study, a RIMS system comprising dye lasers and a time-of-flight mass spectrometer was utilized to investigate even-parity autoionization states within the 300–325 nm range, originating from five excited states within the $3d^8(^3F)4s4p(^3P^o)$ configuration. We have identified 51 even-parity autoionization states in the 64000–66800 cm^{-1} range for the first time, with their relative transition intensities and total angular momentum quantum numbers (J) systematically measured and assigned. These results offer essential spectroscopic input for optimizing two-color two-step photoionization schemes in nickel.

2. Methods

The experimental system comprised a tunable dye laser setup and a time-of-flight mass spectrometer (TOF-MS), as illustrated in Fig. 1.

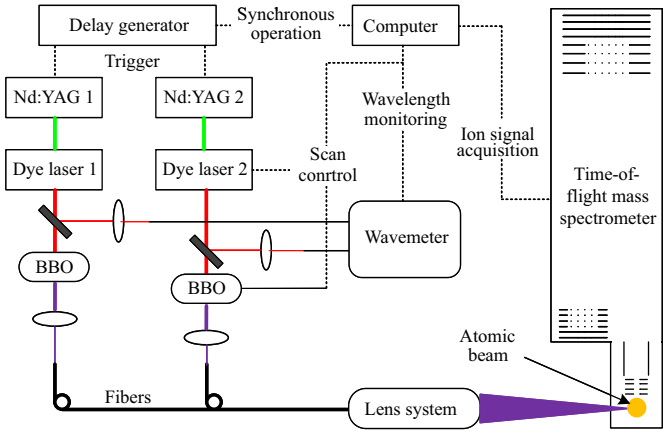


Fig. 1. Schematic diagram of the experimental setup for RIMS of nickel. A computer was connected to a delay generator, a scanning dye laser (with a BBO crystal), a wavemeter, and a mass spectrometer via communication lines (indicated by black dashed lines). The integrated control software enabled synchronized operation, wavelength scanning, real-time monitoring, and ion signal acquisition. Laser beams were transmitted via optical fibers (indicated by black solid lines), shaped by a lens system, and focused onto the nickel atomic beam for resonant ionization. The resulting ions were collected by a time-of-flight mass spectrometer for detection.

The dye laser system was composed of two tunable dye lasers pumped by Nd:YAG solid-state lasers. Each pump laser delivered 532 nm radiation at 10 kHz repetition rate with 50 ns pulse width, and was coupled to the dye lasers via optical fibers. One dye laser was used to pump nickel atoms to excited states, while the other was scanned to probe even-parity autoionization states. The dye lasers, configured with a Littman cavity, generated tunable output spanning 544–658 nm using individually or jointly in-house developed dyes. Each laser typically produced 2 W output power, with a spectral linewidth

of approximately 1.5 GHz and a pulse duration of 20–30 ns. Wavelength tuning and scanning were realized by adjusting the grating position in the Littman cavity via a stepper motor. A small portion of each dye laser beam, extracted outside the laser cavity, was sampled by an optical fiber and directed to a wavelength meter (60 MHz absolute accuracy over 375–800 nm, periodically calibrated with Rb reference lines) for real-time wavelength monitoring, which enabled closed-loop control for fixed-wavelength or step-scanning operation. Both dye laser outputs were frequency-doubled using nonlinear BBO crystals outside the cavity, generating ultraviolet (UV) radiation in the 298–325 nm range, with a maximum power of 200 mW. The frequency-doubling assembly for the scanning laser was designed to automatically adjust its angle based on the wavelength to maintain high conversion efficiency across the broad tuning range. The two laser beams were focused into optical fibers by plano-convex lenses and combined for transmission using a multi-channel fiber combiner, which simplified laser beam combining process compared to conventional setups employing dichroic mirrors. The combiner, equipped with solarization-resistant fibers, achieved a transmission efficiency of approximately 40% for UV light. At the combiner output, an achromatic aspherical mirror assembly shaped the beam into a circular spot of 2.5 mm diameter focused onto the acceleration region of TOF-MS. The mirror assembly with a focal length of 300 mm was fixed in position to suppress potential focal spot drift during long-distance free-space propagation. This design enhanced the stability of the photoionization signal, contributing to improved long-term reproducibility.

The TOF-MS system integrated an atomic evaporation oven and a mass analyzer within a vacuum chamber maintained at 5×10^{-5} Pa. Nickel metal in wire form was loaded into a tantalum capillary within the evaporation oven, where ohmic heating generated the atomic beam at approximately 1400 °C. The atomic beam entered the acceleration region of the mass analyzer through a slit aperture. The acceleration region was configured with pulsed high-voltage repelling electric fields, where photoionization occurred between the positively biased pulsed repelling plate and the grounded plate. The repelling field was triggered by the laser pulse, synchronized at a repetition rate of 10 kHz, with a $\sim$ 300 ns delay between photoionization and the repelling field to suppress Stark effect. The laser propagation direction, atomic beam direction, and ion repulsion direction were arranged orthogonally to minimize Doppler broadening, resulting in a residual Doppler broadening of less than 100 MHz. The photoions underwent three reflections in the mass analyzer before reaching the detector, with signals displayed as mass spectral peaks on an industrial computer, and a mass resolution $M/\Delta M$ (FWHM) exceeding 8000 was achieved. Throughout the experiments, ion signals from ^{58}Ni were primarily recorded. Laser wavelength and mass spectral signals were simultaneously acquired: a distinct increase in signal intensity was observed when the scanned laser wavelength matched the transition from the excited state to the autoionization state, thereby enabling identification of the autoionization transition wavelength. In the absence of autoionization transitions, weak signals from non-resonant ionization of excited states were observed as baseline references.

Figure 2 illustrates the schematic diagram of relevant transitions and energy ranges of autoionization states investigated in this study. The initial level used was $3d^9(^2D)4s\ ^3D_3$ at 204.787 cm^{-1}, which had substantial thermal population at $\sim$ 1400 °C and allowed transitions to the first excited states. To extract energy levels and total angular momentum (J) information for even-parity autoionization states, five odd-parity excited states from the $3d^8(^3F)4s4p(^3P^o)$ configuration were selected based on the NIST atomic database,[50] having similar energies and consecutive angular momenta (J = 2–4), as listed in Table 1. This allowed cross-validation of autoionization peak signals by scanning the same wavelength range using different excited states, thereby improving the accuracy of energy and angular momenta assignments. Due to the generally short lifetimes of the nickel excited states,[51,52] no delay was introduced between the two laser pulses, in order to maximize autoionization signal intensity. The first-step laser power was set to 10 mW to suppress non-resonant ionization background signals of the $2\lambda_1$ type, thereby improving the signal-to-noise ratio of autoionization peaks. The scanning laser power varied between 50 mW and 150 mW depending on the wavelength, and the scanning step size was fixed at 1 pm/s. Maintaining a relatively low laser power was essential to suppress power broadening of the spectral peaks and to ensure accurate spectral characterization.

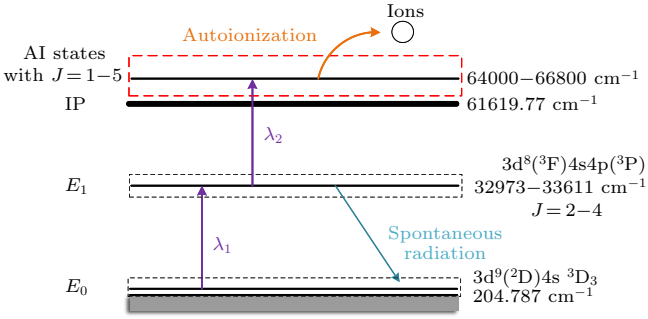


Fig. 2. Schematic diagram of the two-color two-step scheme in atomic nickel and corresponding energy ranges of the even-parity autoionization states investigated in this study.

Table 1. Selected excited states and corresponding transitions for even-parity autoionization studies.

Number	Configuration	Term	E (cm^{-1})	λ_1 (nm)	P_1 (mW)
1	$3d^8(^3F)4s4p(^3P^o)$	$^3F_4^o$	32973.376	305.170	10
2		$^1G_4^o$	33590.13	299.533	
3		$^3F_3^o$	33112.334	303.882	
4		$^3D_3^o$	33500.822	300.336	
5		$^3D_2^o$	33610.89	299.346	

3. Results and discussion

3.1. Single-color two-step photoionization

Atoms populated in the ground or metastable states could be photoionized by absorbing multiple photons of the same wavelength, a process referred to as single-color photoionization. This process could be divided into two types: the "$\lambda_1 + \lambda_1$" process, in which an atom is resonantly excited by the first photon and then ionized non-resonantly by a second photon; and the resonant "$2\lambda_1$" process, where two photons are simultaneously absorbed to reach autoionization states. Because this process involves only a single laser beam, monochromatic photoionization peaks inevitably appeared in the spectra during two-color two-step scans, complicating the identification of even-parity autoionization states. For nickel, the single-color two-step process was found to dominate within our scanning wavelength range. Lievens *et al.*[37] reported 51 single-color photoionization lines within the 313–335 nm range. The strongest transition was attributed to excitation from the ground state to the odd-parity excited state $3d^8(^3F)4s4p(^3P^o)\ ^3G_4^o$ at 30979.749 cm^{-1}, with cross-sections comparable to those observed in two-color two-step photoionization. Therefore, prior to scanning for even-parity autoionization states, it was necessary to account for and exclude interference from single-color two-step photoionization.

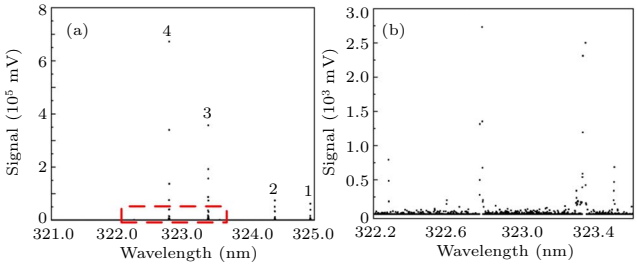


Fig. 3. Single-color photoionization spectrum of atomic nickel in the 321–325 nm range. (b) A magnified view of the red-framed region in (a). The strong peaks labeled 1–4 are listed in Table 2, while the minor peaks with signal intensities below 1000 mV, as shown in (b) with $\lambda = 322.259$ nm and 323.560 nm, are not included.

Table 2. Assigned single-color photoionization lines and corresponding transitions of atomic nickel. ΔE represents the deviation between experimental energies and NIST reference data.[50] The photon energy is given with an experimental error of 0.2 cm^{-1}.

Number	λ (nm)	Photon energy (cm^{-1})	Signal (arb. units)	E-lower (cm^{-1})	E-upper (cm^{-1})	ΔE (cm^{-1})
1	324.939	30775.01	7.93	204.787	30979.75	–0.06
2	324.399	30826.24	11.20	204.787	31031.02	0.00
3	323.386	30922.80	54.56	0	30922.73	–0.09
4	322.793	30979.61	100.00	0	30979.75	0.10
5	319.804	31269.15	0.09	1713.087	32982.26	0.04
6	318.529	31394.32	1.19	2216.55	33610.89	0.03
7	313.501	31897.82	0.07	1713.087	33610.89	0.00
8	311.503	32102.42	0.39	879.816	32982.26	0.02
9	310.278	32229.16	0.09	3409.937	35639.12	0.06
10	310.246	32232.49	4.88	879.816	33112.33	–0.01
11	310.231	32234.04	0.28	0	64468.29	0.18
12	309.801	32278.79	0.11	1332.16	33610.89	–0.07
13	305.850	32695.77	2.90	1713.087	34408.56	–0.18
14	305.518	32731.30	4.75	879.816	33610.89	–0.18
15	303.881	32907.62	0.13	204.787	33112.33	–0.08

We systematically scanned the single-color two-step photoionization spectrum of atomic nickel over the 300–325 nm range. A representative spectrum within the 321–325 nm range, featuring four strong peaks and several weaker ones, was presented in Fig. 2. Fifteen peaks with signal intensities exceeding 1000 mV were recorded across the 25 nm scan range, as only strong peaks were expected to interfere with the identification of even-parity autoionization states. According to the NIST database, all transitions except that at $\lambda = 310.231$ nm corresponded to known transitions from the ground or metastable states to intermediate levels, with a discrepancy below 0.2 cm^{-1}. The measured results show no significant systematic deviation, which can be attributed to the use of a calibrated high-accuracy wavemeter, a fine wavelength scanning step size, and a system design that minimizes contributions from factors such as the Stark effect. Subsequent studies of even-parity autoionization states revealed that the peak at $\lambda = 310.231$ nm originated from a two-photon

transition from the ground state to the autoionization state at 64468.29 cm^{-1}. Signal intensities were normalized to the laser power. The results are summarized in Table 2 relative to the strongest transition ($\lambda = 322.793$ nm) within the scan range. During subsequent two-color scans, these 15 peaks were directly excluded to facilitate the identification of genuine even-parity autoionization states.

Seven single-color two-step transitions above 313 nm in our study exhibited single-photon energies consistent with those reported by Lievens *et al.*,[37] with a maximum discrepancy below 0.1 cm^{-1}. However, our spectrum lacked the numerous unidentified peaks with significant intensities reported in Lievens' work, and the relative intensities showed only semi-quantitative agreement. This discrepancy was likely due to differences in both atomic beam generation methods and laser power. In Lievens' experiment, the ion-sputtered atomic beam may have populated higher energy levels,[53,54] whereas our Ohmic-heated beam, operating under quasi-thermal equilibrium at $\sim$ 1400 °C, concentrates more than 90% of atomic populations in the four lowest energy levels, with negligible populations above 3500 cm^{-1}. Additionally, the single-pulse laser fluence in our study was below 1 mJ/cm^2 — approximately 1% of that reported in the literature. Under high-power laser conditions, atoms could be directly pumped to autoionization states, and transitions with large cross-sections may have reached saturation, while others remained unsaturated, leading to deviations in relative intensities. Our measured relative intensities are likely closer to their true values, as all transitions remain unsaturated under our low laser power conditions. In comparison, the photoionization spectra reported under high-power conditions exhibit significant power broadening, resulting in peak shapes that are markedly wider than those in our measurements. The reduced broadening in our spectra also allows for the determination of peak positions with improved uncertainty.

3.2. Two-color two-step photoionization

Following the identification of potential single-color photoionization interference peaks, the two-color photoionization spectra in the 300–325 nm range were scanned using the excited states listed in Table 1. Figure 4 presents the autoionization spectra in the 64400–64600 cm^{-1} range, where panels (a)–(c) show the results of scans from the excited states numbered 1, 3, and 5 in Table 1, respectively. Within this range, scans from excited states with the same J value — specifically those labeled 1 and 2, and 3 and 4 in Table 1 — produced consistent autoionization features. Thus, representative scans from only one state per group were selected.

After excluding single-color photoionization peaks (marked by red asterisks and numbers in Fig. 4), scans over the same wavelength range from excited states with different J values revealed even-parity autoionization states exhibiting consistent energies, similar line shapes, and varying transition intensities. As shown in Fig. 4(b), all autoionization states observed from the state at 33112.334 cm^{-1} were also confirmed in scans from the other two levels. This multi-excitation-state cross-validation strategy provides strong evidence for the validity of the observed even-parity autoionization states.

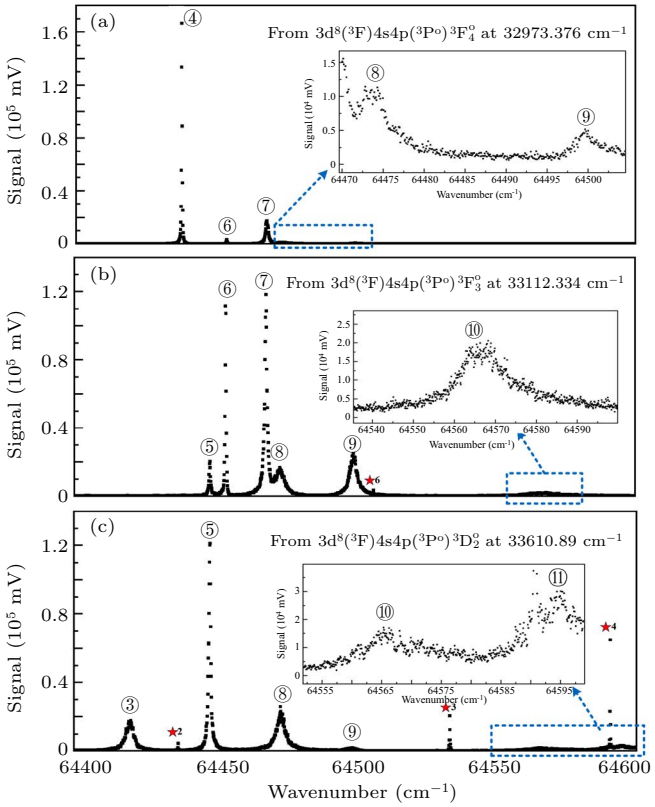


Fig. 4. Autoionization spectra of atomic nickel in the 64400–64600 cm^{-1} range. Panels (a)–(c) show spectra obtained by scanning from three different excited states, respectively. A total of 9 autoionization states were newly identified in this range, labeled ③–⑪, consistent with the numbering in Table 3. Autoionization states with weaker transition intensities highlighted by the blue boxes are shown in the inset subfigures. Identified single-color photoionization peaks are marked with red asterisks and labeled with numbers corresponding to Table 2.

Several broad autoionization states were observed, highlighted by blue boxes in Figs. 4(b) and 4(c). The central positions of these broad peaks could not be directly determined. To compare autoionization spectra obtained from different highly excited states and extract accurate level energies and full-width at half-maximum (FWHM), all autoionization peak data were fitted using the Fano profile[55]

$$I = I_0 \frac{(\varepsilon + q)}{\varepsilon^2 + 1} + I_1, \tag{1}$$

where $\varepsilon = 2(E - E_0)/\Gamma$, E_0 is the central position of peak, Γ is the FWHM, I_1 represents the signal of non-resonant ionization, and q is the Fano parameter describing the asymmetry of the resonance line shape. A representative Fano fitting result is shown in Fig. 5. The scan from the excited state at 32973.376 cm^{-1} revealed three autoionization states in the 65410–65510 cm^{-1} range: two narrow peaks and one broad

peak. These three peaks were fitted with Fano profiles to extract parameters including central positions, FWHMs, and q values. The autoionization state at 65423.43 cm^{-1} exhibited a typical asymmetric Fano profile, with a fitted $q < 10$, suggesting possible interaction with nearby autoionization states, such as No. 28 in Table 3 (65427.82 cm^{-1}), which also showed an asymmetric shape. In contrast, autoionization states exhibiting symmetric Lorentzian line shapes typically interact only with continuum states.

Fano fitting proved essential for accurately determining the central energies of broad peaks. For example, the broad peak at 65462.86 cm^{-1} in Fig. 5, which showed a slightly asymmetric line shape, was scanned three times, and Fano fitting yielded a peak center uncertainty of 0.23 cm^{-1}. In comparison, estimating the peak center using the maximum signal position without fitting resulted in a deviation exceeding 0.5 cm^{-1}. Therefore, all scanned spectral peaks were subjected to Fano fitting to ensure accurate determination of their central positions. Most even-parity autoionization states exhibited symmetric line shapes. Only 10 of them showed pronounced asymmetry and are labeled with the superscript "F" in Table 3.

Each autoionization transition was scanned at least three times, and independent fittings were performed to obtain averaged peak parameters, including the central position, FWHM, and q value. Most transitions exhibited excellent reproducibility in central position, with variations within $\pm$0.3 cm^{-1} across repeated measurements. For broad peaks with widths exceeding 10 cm^{-1} and low signal intensities, the central position uncertainties obtained from fitting reached 1–2 cm^{-1}, mainly due to long-term fluctuations in laser power and atomic beam flux, which altered the peak profiles during scanning. In contrast, broad peaks with higher signal intensities, such as the autoionization state at 65462.86 cm^{-1} shown in Fig. 5, were less susceptible to these fluctuations.

For even-parity autoionization states with consistent energies derived from different excited states, the fitted FWHM values differed by no more than 1.5 cm^{-1}, supporting the validity of the identified autoionization levels. Additionally, the averaged level energies obtained from multiple excited states were highly consistent, with a maximum deviation of approximately 0.5 cm^{-1}.

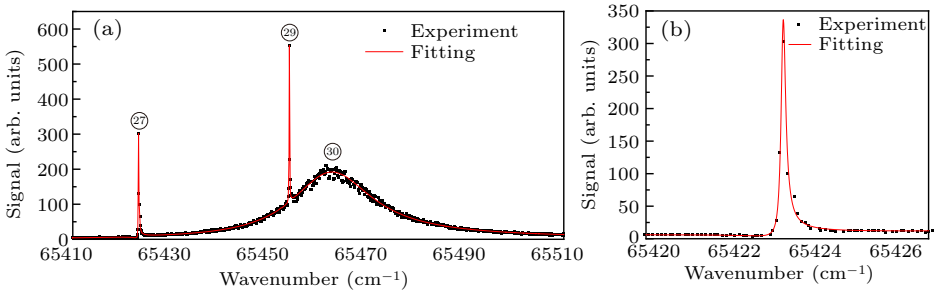


Fig. 5. The even-parity autoionization states in the 65410–65510 cm^{-1} range, observed by scanning from the excited state at 32973.376 cm^{-1}. The red line shows the Fano fitting result. Three autoionization states are present in this range, corresponding to Nos. 27, 29, and 30 in Table 3. The autoionization state at 65423.43 cm^{-1} exhibits a typical asymmetric line shape, with detailed features displayed in panel (b).

All 51 even-parity autoionization states identified in this work are listed in Table 3. With the exception of the $J = 1$ autoionization states and a few near scanning boundaries, most autoionization states were reproducibly observed from multiple excited states. Based on the average level widths, these states were categorized into three groups: broad (B, $>$ 5 cm^{-1}), medium (M, 1–5 cm^{-1}), and narrow (N, $<$1 cm^{-1}). For "N" and "M" autoionization states, the level energies exhibited excellent consistency, with uncertainties below 0.2 cm^{-1}. In contrast, the "B" states showed larger deviations in fitted central positions, with estimated uncertainties up to 2 cm^{-1}. The uncertainties reported in this work are generally consistent with those in previous studies of autoionizing states,[45,48,56,57] primarily due to careful system design that minimized broadening effects such as Doppler, collisional, and power broadening. For broad peaks with relatively weak transition strengths, the uncertainties of level energies determination remain limited by long-term fluctuations in laser power and atomic beam density. Nevertheless, the uncertainty was maintained within 10% of the corresponding linewidth. The uncertainty level achieved here is representative of the upper performance limit for current multimode pulsed dye laser-based measurements.

Angular momentum quantum numbers were uniquely assigned through the $\Delta J = 0, \pm 1$ electric dipole transition rules, based on correlations between the correlating initial excited states and the observed autoionization states. The uniquely determined angular momentum values of the autoionization states are provided in Table 3. Notably, three autoionization states at 65353.87 cm^{-1}, 65427.82 cm^{-1}, and 66784.41 cm^{-1} were observed only in scans from the two $J = 3$ excited states, and thus could not be assigned unique angular momentum values. Their possible J values include 2, 3 or 4. This is likely due to the small transition cross-sections from the selected $J = 2$ and $J = 4$ excited states to these autoionization states, rendering them undetectable under the low laser power conditions used in this experiment. Additionally, the small transition cross-sections may have also contributed to partial in-

consistencies between the $J = 3$ and $J = 4$ excitation datasets. Further scans using additional excited states are required to achieve definitive angular momentum assignments.

Based on the identified even-parity autoionization states, the single-color two-step photoionization transitions listed in Table 2 can be further analyzed. Notably, the unassigned peak at $\lambda = 310.231$ nm (No. 11) is now conclusively attributed to a two-photon transition from the ground state to the even-parity autoionization state at 64468.29 cm^{-1}. The peak at $\lambda = 318.529$ nm (No. 6) arises from a two-step transition: first from 2216 cm^{-1} to 33610.89 cm^{-1}, followed by photon absorption to the even-parity autoionization state at 65004.38 cm^{-1}. This resonant multi-step excitation mechanism explains its anomalously high intensity despite the small thermal population in the 2216 cm^{-1} state. A similar mechanism is proposed for the peak at 305.518 nm (No. 14), where a broad autoionization state at 66339.64 cm^{-1} lies near the transition endpoint. However, the three strongest single-color transitions do not exhibit adjacent autoionization states near their transition endpoints, and their underlying photoionization mechanisms remain uncertain and require further investigation.

Table 3. Experimentally identified even-parity autoionization states. The tabulated energy positions are mean values obtained from repeated scans using different excited states and Fano fitting analyses. The autoionization states are classified by width into three groups: broad (B, > 5 cm^{-1}), medium (M, 1–5 cm^{-1}), and narrow (N, < 1 cm^{-1}). Estimated energy uncertainties are below 2 cm^{-1} for B states and below 0.2 cm^{-1} for M and N states. Angular momentum assignments were determined via cross-scans using the excited states labeled in Table 1, and the corresponding excited states are provided in the last column. States exhibiting strong asymmetric line shapes are labeled with the superscript "F".

Number	E (cm^{-1})	Width	J-value	The excited states from which transitions were observed	Number	E (cm^{-1})	Width	J-value	The excited states from which transitions were observed
1	64074.85	N	5	1	27	65423.43^{F}	N	4	1,3,4
2	64238.61	M	4	1,3	28	65427.82^{F}	N	2/3/4	3,4
3	64419.93	M	1	5	29	65454.08	N	5	1,2
4	64437.83	N	5	1,2	30	65462.86	B	4	1,2,3,4
5	64448.28	N	2	3,4,5	31	65852.28	M	2	3,4,5
6	64453.89	N	4	1,2,3,4	32	65895.40	N	3	2,3,4,5
7	64468.29	M	4	1,2,3,4	33	66112.30	N	5	1
8	64473.54	M	3	1,2,3,4,5	34	66215.43	N	4	1,2,3,4
9	64499.46^{F}	M	3	1,2,3,4,5	35	66263.16	B	1	5
10	64565.91	B	2	3,4,5	36	66294.52	N	5	1,2
11	64595.62	B	1	5	37	66310.12	M	2	3,4,5
12	64857.31^{F}	M	2	3,4,5	38	66320.40^{F}	N	3	2,3,4,5
13	64962.23	N	4	2.3.4	39	66327.88	M	4	2,3,4
14	65004.38	M	2	3,4,5	40	66338.90^{F}	N	4	2,3,4
15	65028.13	M	3	1,2,3,4,5	41	66339.64	B	1	5
16	65030.40	B	1	5	42	66346.90	N	5	2
17	65061.32^{F}	N	3	1,2,3,4,5	43	66374.32^{F}	B	3	2,3,4,5
18	65067.32	B	3	1,2,3,4,5	44	66381.97^{F}	B	2	3,5
19	65107.92	B	1	5	45	66414.19	M	2	3,4,5
20	65136.81	B	3	1,3,4,5	46	66595.61	B	3	2,4,5
21	65210.45	M	4	1,2,3,4	47	66735.81	M	2	4,5
22	65239.84	B	3	1,2,3,4,5	48	66758.01	B	2	4,5
23	65348.08	N	4	1,2,3,4	49	66784.71^{F}	M	2/3/4	4
24	65353.87	B	2/3/4	3,4	50	66789.78	N	4	2,4
25	65361.14	M	5	1,2	51	66797.89	M	5	2
26	65385.23	B	2	3,4,5					

To design more efficient two-color photoionization pathways, a systematic comparison of transition intensities from various excited states to even-parity autoionization states was performed to identify transitions with high photoionization cross-sections. The maximum photoionization cross-section reported for a two-color two-step photoionization pathway by Lievens *et al.*[37] is 6.5×10^{-16} cm^2. The laser power required to measure the saturation curve of such autoionization transitions is estimated to be on the order of tens of watts, which far exceeds the output capacity of our dye laser system. During our scans, conducted at a maximum laser power of 150 mW, the autoionization transitions remained within the linear region of the saturation curve. Consequently, laser-power-normalized signal intensities from the same excitation pathways were used to compare relative transition strengths. Meanwhile, the strong single-color two-step photoionization transitions listed in Table 2 were consistently observed across all excited state scans. The strongest of these, at $\lambda = 322.793$ nm, has an ionization cross-section of 4×10^{-16} cm^2,[37] and serves as a reference for comparing photoionization transition intensities from different excited states. For the five selected excited states, the signal intensities of autoionization transitions were first normalized to the scanning laser power. Then, using the transition $\lambda = 322.793$ nm as the

reference (with its relative transition intensity value set to 100, as in Table 2), the relative transition intensities of autoionization transitions from different excited states were calculated to guide the design of efficient two-color two-step photoionization pathways. This analysis revealed that most autoionization transitions exhibited relative intensities below 100, while only five transitions showed relative intensities exceeding 250. These transitions likely possess ionization cross-sections on the order of 10^{-15} cm^2. Table 4 summarizes the wavelengths and relative intensities of these five strong transitions, while all the datasets, including wavelengths, level energies, FWHM, and relative transition intensities for all 141 autoionization transitions, are compiled in the supplementary materials (SM).

The transition originating from the excited state at 33590.13 cm^{-1} to the autoionization state at 64437.77 cm^{-1} has the largest ionization cross-section in this work. This two-color two-step photoionization pathway is well-suited for CRIS studies of unstable nickel nuclei, as its transition cross-section is significantly larger than that of previously reported pathways. Moreover, it requires only low laser power to achieve transition saturation, thereby allowing further miniaturization of the laser system. The pathway also exhibits excellent flexibility, as the selected excited state can be accessed from both the ground and first metastable states. Notably, a three-color two-step photoionization pathway can be devised, in which both the ground and the lowest metastable states are first pumped to 33590.13 cm^{-1}, followed by efficient photoionization using a $\lambda = 324.174$ nm laser. This pathway is expected to yield the most intense nickel photoionization signal.

Table 4. The strongest autoionization transitions identified through spectral scanning.

Number	E (cm^{-1})	λ_1 (nm)	E_1 (cm^{-1})	λ_2 (nm)	E_2 (cm^{-1})	Relative transition intensity
1		299.533	33590.13	324.174	64437.77	795
2		300.336	33500.822	317.850	64962.22	543
3	204.787	300.336	33500.822	322.919	64468.30	497
4		305.170	32973.376	308.884	65348.03	299
5		303.882	33112.334	313.972	64962.28	260

4. Conclusions

This study utilized resonance ionization mass spectrometry (RIMS) to investigate single-color photoionization processes of atomic nickel in the 300–325 nm spectral range. Fifteen intense single-color transitions were identified as potential interference peaks for subsequent two-color studies. By comparing scan results from five odd-parity excited states, 51 even-parity autoionization states in the 64000–668000 cm^{-1} range were identified for the first time, with unique angular momentum values determined for 48 of them. Using the strongest single-color photoionization line at $\lambda = 322.793$ nm as a reference, the transition from the excited state $3d^8(^3F)4s4p(^3P^o)\ ^1G_4^o$ at 33590.13 cm^{-1} to the autoionization state at 64437.77 cm^{-1} has the largest ionization cross-section, which may serve as an optimized two-color two-step photoionization pathway for CRIS studies of unstable nickel nuclei. This work expands the known region of even-parity autoionization states in atomic nickel, providing valuable data for the theoretical modeling of atomic autoionization.

Data availability statement

The data that support the findings of this study are openly available in Science Data Bank at https://doi.org/10.57760/sciencedb.j00113.00280.

Acknowledgement

This work was supported by the China National Nuclear Corporation Basic Research Project (Grant No. CNNC-JCYJ-202327).

References

[1] Ye Y, Yang X, Sakurai H and Hu B 2024 *Nat. Rev. Phys.* **7** 21
[2] Yang X F, Wang S J, Wilkins S G and Ruiz R F G 2023 *Prog. Part. Nucl. Phys.* **129** 104005
[3] Sorlin O and Porquet M G 2008 *Prog. Part. Nucl. Phys.* **61** 602
[4] Sommer F, König K, Rossi D M, *et al.* 2022 *Phys. Rev. Lett.* **129** 132501
[5] Pineda S V, König K, Rossi D M, Brown B A, Incorvati A, Lantis J, Minamisono K, Nörtershäuser W, Piekarewicz J, Powel R and Sommer F 2021 *Phys. Rev. Lett.* **127** 182503
[6] König K, Sommer F, Lantis J, Minamisono K, Nörtershäuser W, Pineda S and Powel R 2021 *Phys. Rev. C* **103** 054305
[7] Kaufmann S, Simonis J, Bacca S, *et al.* 2020 *Phys. Rev. Lett.* **124** 132502
[8] Taniuchi R, Santamaria C, Doornenbal P, *et al.* 2019 *Nature* **569** 53
[9] Sun X H, Wang H, Yoneda K, *et al.* 2024 *Phys. Lett. B* **858** 139081
[10] Malbrunot-Ettenauer S, Kaufmann S, Bacca S, *et al.* 2022 *Phys. Rev. Lett.* **128** 022502
[11] Hosmer P T, Schatz H, Aprahamian A, *et al.* 2005 *Phys. Rev. Lett.* **94** 112501
[12] Koszorús Á and Cheal B 2024 *Eur. Phys. J. Spec. Top.* **233** 1133
[13] Koszorús Á, De Groote R P, Cheal B, Campbell P and Moore I D 2024 *Eur. Phys. J. A* **60** 20
[14] Campbell P, Moore I D and Pearson M R 2016 *Prog. Part. Nucl. Phys.* **86** 127
[15] De Groote R P, Budinčević I, Billowes J, *et al.* 2015 *Phys. Rev. Lett.* **115** 132501
[16] Farooq-Smith G J, Vernon A R, Billowes J, Binnersley C L, Bissell M L, Cocolios T E, Day Goodacre T, De Groote R P, Flanagan K T, Franchoo S, Garcia Ruiz R F, Gins W, Lynch K M, Marsh B A, Neyens G, Rothe S, Stroke H H, Wilkins S G and Yang X F 2017 *Phys. Rev. C* **96** 044324

[17] Lynch K M, Wilkins S G, Billowes J, *et al.* 2018 *Phys. Rev. C* **97** 024309

[18] Koszorús Á, Yang X F, Billowes J, Binnersley C L, Bissell M L, Cocolios T E, Farooq-Smith G J, De Groote R P, Flanagan K T, Franchoo S, Garcia Ruiz R F, Geldhof S, Gins W, Kanellakopoulos A, Lynch K M, Neyens G, Stroke H H, Vernon A R, Wendt K D A and Wilkins S G 2019 *Phys. Rev. C* **100** 034304

[19] De Groote R P, Billowes J, Binnersley C L, *et al.* 2020 *Nat. Phys.* **16** 620

[20] Garcia Ruiz R F, Berger R, Billowes J, *et al.* 2020 *Nature* **581** 396

[21] Gustafsson F P, Ricketts C M, Reitsma M L, Garcia Ruiz R F, Bai S W, Berengut J C, Billowes J, Binnersley C L, Borschevsky A, Cocolios T E, Cooper B S, De Groote R P, Flanagan K T, Koszorús Á, Neyens G, Perrett H A, Vernon A R, Wang Q, Wilkins S G and Yang X F 2020 *Phys. Rev. A* **102** 052812

[22] Vernon A R, Ricketts C M, Billowes J, Cocolios T E, Cooper B S, Flanagan K T, Garcia Ruiz R F, Gustafsson F P, Neyens G, Perrett H A, Sahoo B K, Wang Q, Waso F J and Yang X F 2020 *Sci. Rep.* **10** 12306

[23] Koszorús Á, Yang X F, Jiang W G, *et al.* 2021 *Nat. Phys.* **17** 439

[24] Bai S W, Koszorús Á, Hu B S, *et al.* 2022 *Phys. Lett. B* **829** 137064

[25] Vernon A R, Garcia Ruiz R F, Miyagi T, Binnersley C L, *et al.* 2022 *Nature* **607** 260

[26] Johnson J D, Heines M, Bruchertseifer F, Chevallay E, Cocolios T E, Dockx K, Duchemin C, Heinitz S, Heinke R, Hurier S, Lambert L, Leenders B, Skliarova H, Stora T and Wojtaczka W 2023 *Sci. Rep.* **13** 1347

[27] Savina M R, Isselhardt B H, Shulaker D Z, Robel M, Conant A J and Ade B J 2023 *Sci. Rep.* **13** 5193

[28] Kaja M, Studer D, Berg F, Berndt S, Düllmann C E, Kneip N, Reich T, Urquiza-González M and Wendt K 2024 *Eur. Phys. J. D* **78** 50

[29] Miyabe M, Iwata Y, Tomita H, Morita M and Sakamoto T 2024 *Spectroc. Acta Pt. B-Atom. Spectr.* **221** 107036

[30] Lantis J, Claessens A, Münzberg D, *et al.* 2024 *Phys. Rev. Res.* **6** 023318

[31] Raiwa M, Savina M R, Roberts A G, Shulaker D Z and Isselhardt B H 2024 *J. Am. Soc. Mass Spectrom.* **35** 3233

[32] Jokinen A, Evensen A H, Kugler E, Lettry J, Ravn H, Van Duppen P, Erdmann N, Jading Y, Köhler S, Kratz K L, Trautman N, Wöhr A, Fedoseyev V N, Mishin V I and Tikhonov V 1997 *Nucl. Instrum. Methods Phys. Res. Sect. B-Beam Interact. Mater. Atoms* **126** 95

[33] Kessler T, Brück K, Baktash C, Beene J R, Geppert C, Havener C C, Krause H F, Liu Y, Schultz D R, Stracener D W, Vane C R and Wendt K 2007 *J. Phys. B-At. Mol. Opt. Phys.* **40** 4413

[34] Shi X, Huang H, Jacobson B, Chang Y C, Yin Q Z and Ng C Y 2012 *ApJ* **747** 20

[35] Tsvetkov G O, D'yachkov A B, Gorkunov A A, Labozin A V, Mironov S M, Firsov V A and Panchenko V Y 2017 *Quantum Electron.* **47** 48

[36] Zhang J Y, Xiong J Y, Zhou H R, Zhu C H, Sun H M, Wang L D, Chai J J and Li Y F 2025 *Spectroc. Acta Pt. B-Atom. Spectr.* **231** 107249

[37] Lievens P, Vandeweert E, Thoen P and Silverans R E 1996 *Phys. Rev. A* **54** 2253

[38] Kim D S and Tayal S S 2000 *J. Phys. B: At. Mol. Opt. Phys.* **33** 3235

[39] Avery J and Avery J 2005 *Adv. Quantum Chem.* **49** 103

[40] Cardona J C and Sanz-Vicario J L 2008 *J. Phys. B: At. Mol. Opt. Phys.* **41** 055003

[41] Argenti L and Moccia R 2016 *Phys. Rev. A* **93** 042503

[42] Baig M A 2022 *Atoms* **10** 39

[43] Vandeweert E, Lievens P, Philipsen V and Silverans R E 1999 *Spectroc. Acta Pt. B-Atom. Spectr.* **54** 1219

[44] Marsh B A 2014 *Rev. Sci. Instrum.* **85** 049901

[45] Rath A D, Biswal D and Kundu S 2021 *J. Quant. Spectrosc. Radiat. Transf.* **270** 107696

[46] Zhang J Y, Xiong J Y, Wei S Q, Li Y F and Lu X Y 2023 *Acta Phys. Sin.* **72** 193203 (in Chinese)

[47] Iwata Y, Miyabe M, Akaoka K, Wakaida I and Hasegawa S 2024 *J. Opt. Soc. Am. B* **41** 119

[48] Zhang J Y, Lu X Y, Li Y F and Chai J J 2024 *Eur. Phys. J. D* **78** 95

[49] Meher L P, Kumar V, Biswal D and Rath A D 2025 *J. Quant. Spectrosc. Radiat. Transf.* **331** 109273

[50] Kramida A, Ralchenko Yu, Reader J, NIST ASD Team 2024 *NIST Atomic Spectra Database* (ver. 5.12) [Online]. 2025 May 24, Gaithersburg, MD: National Institute of Standards and Technology. DOI:10.18434/T4W30F

[51] Bergeson S D and Lawler J E 1993 *J. Opt. Soc. Am. B* **10** 794

[52] Shang X, Wang Q, Zhang F, Wang C and Dai Z 2015 *J. Quant. Spectrosc. Radiat. Transf.* **163** 34

[53] Vernon A R, Billowes J, Binnersley C L, Bissell M L, Cocolios T E, Farooq-Smith G J, Flanagan K T, Garcia Ruiza R F, Gins W, de Groot R P, Koszorús Á, Lynch K M, Neyens G, Ricketts C M, Wendt K D A, Wilkins S G and Yang X F 2019 *Spectroc. Acta Pt. B-Atom. Spectr.* **153** 61

[54] Mushtaq S 2022 *J. Anal. At. Spectrom.* **37** 985

[55] Fano U 1961 *Phys. Rev.* **124** 1866

[56] Mandal P K, Sahoo A C, Das R C, Shah M L and Dev V 2017 *Appl. Phys. B* **123** 192

[57] Sahoo A C, Mandal P K, Mukherjee J, Dev V and Shah M L 2021 *J. Quant. Spectrosc. Radiat. Transf.* **276** 107944